

NASA Technical Memorandum 103846

20333

P 15

Application of Higher Harmonic Control to Hingeless Rotor Systems

Khanh Nguyen and Inderjit Chopra

(NASA-TM-103846) APPLICATIONS OF HIGHER
HARMONIC CONTROL TO HINGELESS ROTOR SYSTEMS
(NASA) 15 P CSCL 01B

N91-25102

Unclas
G3/01 0020333

March 1991

NASA

National Aeronautics and
Space Administration

[

2011年11月11日

Application of Higher Harmonic Control to Hingeless Rotor Systems

Khanh Nguyen, Ames Research Center, Moffett Field, California

Inderjit Chopra, University of Maryland, College Park, Maryland

March 1991



National Aeronautics and
Space Administration

Ames Research Center
Moffett Field, California 94035-1000



APPLICATION OF HIGHER HARMONIC CONTROL TO HINGELESS ROTOR SYSTEMS

Khanh Nguyen*[†]

Inderjit Chopra[‡]

[†]Rotorcraft Aeromechanics Branch, NASA Ames Research Center, Moffett Field CA 94035

[‡]Center for Rotorcraft Education and Research, Department of Aerospace Engineering, University of Maryland, College Park, Maryland 20742

Abstract- A comprehensive analytical formulation has been developed to predict the vibratory hub loads of a helicopter rotor system in forward flight. The analysis is used to calculate the optimal higher harmonic control inputs and associated actuator power required to minimize these hub loads. The present formulation is based on a finite element method in space and time. A nonlinear time domain, unsteady aerodynamic model is used to obtain the airloads, and the rotor induced inflow is calculated using a nonuniform inflow model. Predicted vibratory hub loads are correlated with experimental data obtained from a scaled model rotor. Results of a parametric study on a hingeless rotor show that blade flap, lag and torsion vibration characteristics, offset of blade center of mass from elastic axis, offset of elastic axis from quarter-chord axis, and blade thrust greatly affect the higher harmonic control actuator power requirement.

1. INTRODUCTION

Higher harmonic control (HHC) is an attractive concept to alleviate helicopter vibration where the vibration is eliminated at the source. The primary source of helicopter vibration is the aerodynamic input of the individual rotor blades, which is influenced in turn by the environment at the rotor disk. The oscillatory aerodynamic and inertial loads from the rotating blades are transmitted as exciting forces and moments at the hub to the airframe at a dominant frequency of N per rev, where N is the number of rotor blades. An HHC system is an active vibration control device, wherein the blades are oscillated at higher harmonics of the rotor rotational speed. There are several ways to implement HHC on a rotor system, and the most popular approach is blade feathering at the root using swashplate oscillations. Using high frequency servo-actuators, the swashplate is excited in the fixed system in the collective, and longitudinal and lateral cyclic modes at N per rev, with resulting blade pitch oscillations at three distinct frequencies of $N-1$, N , and $N+1$ per rev in the rotating frame. If these blade pitch oscillations are applied appropriately, they will generate a combination of unsteady aerodynamic and inertial loads to counteract the existing vibratory blade loads which cause airframe vibration. With advances in servo-actuator technology and the availability of high speed microprocessors, there appears to be great potential for HHC as an effective approach to control helicopter vibration under varying flight conditions.

HHC has been investigated by many researchers using numerical simulation [1-3], model testing in wind tunnels [4-6], and full-scale flight testing [7-9]. These studies have been carried out on a number of different rotor systems and showed that HHC produced substantial reductions in vibratory hub loads. Also, HHC has been implemented successfully using various types of feedback controllers (see Ref. 10 for review). It has been found that the higher harmonic blade pitch needed to suppress vibrations is reasonable (typically less than 2°), and therefore the power requirements for the actuators are manageable. However, most of the existing studies have been confined to articulated rotor systems. With the growing acceptance of using composite materials in the construction of rotor blades, future helicopters are moving toward hingeless rotor designs for better maneuverability and maintenance characteristics. Because hingeless rotor helicopters are susceptible to higher levels of vibration, it is important to study the means to alleviate vibration for these rotor systems.

The present paper uses a comprehensive analysis to examine the problems associated with the implementation of HHC to reduce vibratory hub loads for hingeless rotors. Unlike articulated rotors, the vibratory rotor hub moments contribute significantly to airframe vibration for hingeless rotors. Thus, the HHC inputs required to suppress vibration for hingeless rotor systems may be larger than those required for articulated rotor systems. Consequently, the actuator power requirement for hingeless rotors may become a critical issue. Indeed, for certain rotor designs, the weight penalty imposed by the actuator system becomes so high as to make the implementation of HHC impractical. The objective of this paper is to make a systematic analytical study to determine the HHC inputs and the associated actuator power required to suppress the vibratory hub loads for hingeless rotor systems under differing flight conditions.

This analytical study was conducted using a comprehensive coupled aeroelastic analysis developed at the Rotorcraft Center, University of Maryland [3,11-13]. The analysis first computes the trim control settings from the vehicle equilibrium equations: three force equations (vertical, longitudinal, and lateral) and three moment equations (roll, pitch, and yaw). A nonlinear time domain, unsteady aerodynamic theory [14,15], which includes both trailing edge separation as well as dynamic stall effects, is used to obtain the blade section lift, drag, and pitching moment. Impulsive (noncirculatory) loads, compressibility effects, and reverse flow correction are included. A free wake model [16] has also been coupled into the analysis to calculate the rotor nonuniform induced inflow. The blade nonlinear periodic responses are solved from normal mode equations using a temporal finite element method. Vehicle trim control settings and rotor blade responses are calculated iteratively as one coupled solution using a modified Newton method. HHC response calculations

*Former Rotorcraft Fellow, Center for Rotorcraft Education and Research, Department of Aerospace Engineering, University of Maryland, College Park, Maryland 20742

form a part of the steady response solution where the basic collective and cyclic pitch inputs are superimposed with the higher harmonic components.

A transfer matrix approach is adopted to relate harmonics of the HHC inputs to harmonics of the vibratory hub loads. Optimal HHC inputs are calculated by minimizing the harmonics of the vibratory hub loads expressed in terms of a quadratic performance index. Using a multiblade coordinate transformation, HHC inputs in the rotating frame are transformed to the fixed frame in terms of swashplate motions. Higher harmonic swashplate motions are generated using a number of auxiliary servo-actuators, and the hydraulic power for the actuators is then calculated for specified HHC inputs [3]. Effects of several blade design parameters on the actuator power are examined including blade flap, lag and torsion stiffnesses, offset of blade center of mass from elastic axis, offset of elastic axis from quarter-chord axis, blade pretwist, blade number, forward speed, and thrust level.

2. FORMULATION

The analysis used in this study is formulated based on the finite element methods both in space and time. It calculates iteratively the vehicle trim control settings and the blade nonlinear response as a coupled solution. For the structural model, the hub is assumed fixed and the blade is considered as an elastic beam undergoing flap bending, lead-lag bending, torsion and axial deflections. A finite element method based on Hamilton's principle is used to discretize the blade into a number of beam elements each having fifteen degrees of freedom. Between the elements, there is a continuity of displacement and slope for flap and lag bending deflections and continuity of displacement for elastic twist and axial deflection. The assembly of beam elements, followed by an application of the boundary conditions, yields the blade equations in terms of nodal displacements which contain nonlinear geometric terms.

2.1 Blade Section Airloads

For accurate prediction of blade response due to higher harmonic forcing, the aerodynamic model must include unsteady as well as nonlinear effects. In the present analysis, blade section airloads can be calculated using either quasi-steady incompressible aerodynamics or a more descriptive nonlinear unsteady aerodynamic formulation. This latter formulation is based on the works of Leishman and Beddoes [14,15] and consists of an attached flow (linear) formulation, including compressibility effects, along with a representation of the nonlinear effects due to flow separation and dynamic stall.

2.1.1. Attached Flow Formulation

In this part of the model, the unsteady lift is assumed to consist of the circulatory and impulsive (noncirculatory) components. The loads are obtained using an indicial response representation [15] along with superposition in the form of a finite difference approximation to the Duhamel's integral. Physically, the circulatory lift includes the time history of the shed wake, and the impulsive lift is due to the presence of pressure waves generated by the airfoil motion. Impulsive loads can be considered as the compressible analog of the apparent mass terms used in the incompressible analyses. An interesting feature of this representation is that the unsteady pressure drag can be computed from the time-dependent lift and chordwise force components [14].

Unsteady aerodynamic pitching moments also consist of circulatory and impulsive components. The circulatory component arises from the offset of the circulatory lift component acting at the aerodynamic center and from the induced camber effects associated with the airfoil pitch rate. As in the case of lift, the time rate of change of angle of attack and pitch rate contribute to both the circulatory and the impulsive moment components.

2.1.2. Trailing Edge Separation

To simulate nonlinear aerodynamic effects associated with trailing edge flow separation, a Kirchhoff flow model is used [14]. This model relates the airfoil nonlinear lift behavior to the position of the trailing edge separation point. This point is defined as the chordwise distance between the airfoil leading edge and the point where the flow starts to detach from the airfoil upper surface. Using Kirchhoff's model, an effective separation point can be inferred from static lift data for a given airfoil at a given Mach number. The variation of the separation point with angle of attack is then curve-fitted and used to reconstruct the airfoil characteristics.

Under unsteady conditions, the position of the separation point is governed by time-dependent effects on the airfoil pressure distribution together with a time-dependent boundary layer response. In addition to a lag in lift with respect to the time history of the angle of attack, there is also a lag in the airfoil unsteady pressure distribution with respect to lift. A representation of this is obtained by applying a first order lag to the instantaneous normal force. This results in an ersatz normal force which is used to estimate a "quasi-steady" separation point for the corresponding unsteady pressure on the airfoil. An additional lag is then applied to this separation point to simulate the dynamics of the boundary layer response to changes in the pressure distribution. The resulting separation point is finally used to calculate the nonlinear lift, drag, and pitching moment.

2.1.3. Dynamic Stall

Physically, dynamic stall is characterized by leading edge separation and the shedding of concentrated vorticity from the leading edge region. This vorticity is swept downstream over the chord and produces significant increments in the airfoil lift, drag, and pitching moment. Dynamic stall onset is modeled using a criterion such that separation is initiated when the ersatz normal force attains a critical value, C_{N_c} , corresponding to a critical leading edge pressure. The value of C_{N_c} corresponds closely to the airfoil maximum static lift coefficient and depends on both the airfoil geometry and Mach number.

Once leading edge separation is initiated, the vortex lift is computed using an incremental lift quantity which is related to the difference in lift between the attached (linear) and separated (nonlinear) flow conditions. As the vortex is swept downstream, the airfoil center of pressure varies with the chordwise position of the vortex. The vortex convection is monitored using a nondimensional time based on the distance traveled by the airfoil in semichords. By monitoring the excess lift and the position of the center of pressure, the vortex induced pitching moment can be calculated. As the vortex reaches the airfoil trailing edge, the excess lift is allowed to decay rapidly, and its effects on the airloads are quickly reduced.

The elements of the model as discussed above are based on a discrete-time representation making the complete aerodynamic model compatible with the temporal finite element technique used in this analysis. With this technique, blade

aeroelastic responses are calculated iteratively, and unsteady aerodynamic loads are computed based on blade response from the previous iteration.

2.2. Rotor Wake Modeling

Calculation of the rotor nonuniform inflow is one of the crucial steps in the prediction of blade aeroelastic responses, blade loads, noise, and rotor performance. An accurate, yet computationally efficient, rotor wake analysis is required for HHC analysis. The free wake analysis of Ref. 16 is adopted to calculate the rotor nonuniform induced inflow. It computes the rotor induced inflow from the vortex wake filaments using the Biot-Savart law. In contrast to prescribed wake models where the wake geometry is known, a self-distorted free wake geometry is calculated in the free wake analysis. To improve computational efficiency, the wake is divided into near wake and far wake regions. The helical geometry of the concentrated tip vortices in the near wake region is computed iteratively while the remaining parts of the wake model are calculated once and held fixed. The contribution of the inboard wake has small but not negligible effects on the prediction of the blade airloads.

Coupling of the free wake model and the aeroelastic analysis is made by transferring blade bound circulation strength, blade motions, and induced inflow between these two analyses. The coupling has been performed in a consistent manner with the current aeroelastic analysis. Furthermore, the shed wake model in the free wake analysis is suppressed since these effects have already been included in the blade section airloads.

2.3. Blade Response and Hub Loads

The solution procedure involves the calculation of the vehicle trim controls, blade steady responses, and hub loads. In the first phase, the rotor trim controls are obtained from the vehicle equilibrium equations. For a given flight condition, the trim procedure calculates the collective and cyclic trim inputs, rotor uniform induced inflow (based on momentum theory), and rotor shaft tilt angles [11].

The second phase involves calculation of the blade steady response for one rotor revolution. Using finite element discretization, the blade governing equations are obtained as a set of nonlinear ordinary differential equations with periodic coefficients. Using six to eight coupled natural vibration modes, these equations are then transformed into the normal mode equations to reduce computation time. Blade steady periodic response is calculated using a finite element in time method based on Hamilton's principle in weak form. In this temporal finite element method, the time period of one rotor revolution is discretized into a number of time elements. For each time element, fifth order Lagrangian polynomials are used as shape functions for the modal displacements. The normal mode nonlinear differential equations with periodic coefficients are transformed into a set of nonlinear algebraic equations which are solved iteratively using a Quasi-Newton method. During the iteration scheme, rotor controls and vehicle orientations are also updated based on the vehicle equilibrium conditions. This control updating scheme is usually referred to as the coupled-trim algorithm.

Once blade response and vehicle control settings are solved, the force summation method is used to calculate rotor hub loads. In this method, the blade section aerodynamic and inertial loads are integrated spanwise to yield the blade root loads. The resulting blade root loads are then summed over all the blades to yield the rotor hub loads in either fixed or rotating frames. Rotor hub loads are harmonically analyzed to obtain the vibratory harmonics.

2.4. HHC System

For vibration control, the blade pitch schedule with HHC becomes

$$\theta(x, \Psi) = \theta_{0.75} + \theta_{tw}(x - 0.75) + \theta_{1c} \cos \Psi + \theta_{1s} \sin \Psi + \sum_{n=N-1}^{N+1} (\theta_{nc} \cos n\Psi + \theta_{ns} \sin n\Psi) \quad (1)$$

where x is the nondimensional radial length; Ψ is the azimuth angle; θ_{tw} is the blade linear pretwist; $\theta_{0.75}$ is the collective pitch angle at 75 percent radius; θ_{1c} and θ_{1s} are respectively the lateral and longitudinal cyclic pitch angles; and θ_{nc} and θ_{ns} are respectively the cosine and sine components of the HHC inputs. The following linear frequency domain global model relating the input pitch harmonics and the output hub load harmonics is assumed:

$$z = z_o + T \theta \quad (2)$$

where the response vector z has 10 components and consists of sine and cosine components of the vibratory hub loads, z_o is the uncontrolled response vector, and T is the transfer matrix. The HHC input vector θ has six components and consists of sine and cosine components of the higher harmonic blade pitch at three distinct frequencies of $N-1$, N and $N+1$ per rev. In this formulation, the transfer matrix is generated using a finite-difference approach.

For minimum vibration, the optimal control input $\dot{\theta}$ is obtained from the minimization of the quadratic performance index J ,

$$\min J = \min \left(\frac{1}{2} z^T W_z z + \frac{1}{2} \theta^T W_\theta \theta \right) \quad (3)$$

subject to

$$z = z_o + T \theta$$

where J is a quadratic performance index, W_z and W_θ are weighting matrices for z and θ respectively. The optimal control $\dot{\theta}$ depends on the type of controller used. Two types of controllers are used in this analysis; open-loop and closed-loop deterministic controllers.

For the open-loop controller, optimal control $\dot{\theta}$ depends only on the uncontrolled response, i.e.

$$\dot{\theta} = C z_o \quad (4)$$

where

$$C = -(T^T W_z T + W_\theta)^{-1} T^T W_z \quad (5)$$

For the closed-loop controller, Eq. (2) is modified for each cycle and is expressed as

$$z_n = z_{n-1} + T(\theta_n - \theta_{n-1}) \quad (6)$$

and the HHC inputs become

$$\theta_n = \theta_{n-1} + Cz_{n-1} \quad (7)$$

This is a closed-loop feedback controller since the responses from the previous cycle are used to update the control inputs.

2.5. Actuator Power Required for an HHC System

To obtain the actuator power required for an HHC system, the optimal HHC inputs are transformed into swashplate motions [17],

$$\begin{Bmatrix} C_{long,c} \\ C_{long,s} \\ C_{col,c} \\ C_{col,s} \\ C_{lat,c} \\ C_{lat,s} \end{Bmatrix} = \begin{bmatrix} 0 & 1 & 0 & 0 & -1 & 0 \\ -1 & 0 & 0 & 0 & 0 & 1 \\ 0 & 0 & 1 & 0 & 0 & 0 \\ 0 & 0 & 0 & 1 & 0 & 0 \\ 0 & 1 & 0 & 0 & 1 & 0 \\ 1 & 0 & 0 & 0 & 0 & 1 \end{bmatrix} \begin{Bmatrix} \theta_{(N-1)c} \\ \theta_{(N-1)s} \\ \theta_{Nc} \\ \theta_{Ns} \\ \theta_{(N+1)c} \\ \theta_{(N+1)s} \end{Bmatrix} \quad (8)$$

where C_{col} , C_{long} , and C_{lat} are the NP swashplate angles in the collective, longitudinal, and lateral modes, respectively, and the subscript "c" refers to cosine component and "s" refers to the sine component.

The actuator power P_R generated by a hydraulic pump is equal to the product of the pump pressure p_e and the average pump flow rate Q_{av} [18],

$$P_R = p_e Q_{av} \quad (9)$$

For HHC application, the pump flow rate must be sufficient to excite the NP swashplate motions resulting in the desired HHC inputs. For a particular actuator design, the flow rate Q depends on the swashplate oscillatory speed and the actuator displacement, i.e.

$$Q = N \Omega S_n A_e \quad (10)$$

where A_e is the effective piston area, and S_n is the actuator displacement. The average pump flow rate Q_{av} is calculated assuming that an accumulator is used to smooth out the flow, thus

$$Q_{av} = \frac{2}{\pi} N \Omega S_n A_e \quad (11)$$

Throughout the helicopter flight regime, the actuators must operate at a constant fluid pressure selected to accommodate the maximum possible pitch link load. Such loads typically occur at severe flight conditions such as a high "g" maneuver or a high speed condition where a major part of the rotor disc is exposed to dynamic stall. Since the maximum pitch link load depends on the vehicle flight conditions, it is assumed in this analysis that the fluid pump pressure is a known constant. Therefore, the actuator power required for an N -bladed rotor is expressed as

$$P_R = \frac{2}{\pi} N^2 \Omega A_e p_e c_n S_n \quad (12)$$

where c_n is a constant dependent on the radial locations of the actuators and the pitch link, and S_n is the accumulation index for the swashplate higher harmonic motion amplitudes. If the swashplate is oscillated using four equally spaced hydraulic actuators, then S_n can be expressed as

$$S_n = \sqrt{(C_{col,c} + C_{lat,c})^2 + (C_{col,s} + C_{lat,s})^2} + \sqrt{(C_{col,c} + C_{long,c})^2 + (C_{col,s} + C_{long,s})^2} \\ + \sqrt{(C_{col,c} - C_{lat,c})^2 + (C_{col,s} - C_{lat,s})^2} + \sqrt{(C_{col,c} - C_{long,c})^2 + (C_{col,s} - C_{long,s})^2} \quad (13)$$

The actuator power for an HHC system is therefore dependent on the number of blades, the rotor rotational speed, the hydraulic pump pressure and diameter, the locations of the pitch links and actuators, and the HHC inputs. Since most of these parameters are fixed for a given rotor design, the associated actuator power is conveniently represented by a power index defined as

$$P_I = \frac{P_R}{(2/\pi) N^2 \Omega A_e p_e c_n} \quad (14)$$

This gives

$$P_I = S_n \quad (15)$$

Thus, for a given actuator design and pitch-link configuration, the actuator power depends only on the swashplate motions and is directly related to the HHC inputs.

3. RESULTS AND DISCUSSION

3.1. Correlation with Wind Tunnel Data

To validate the analysis, a correlation study of predicted vibratory hub loads with experimental data was carried out. The data were obtained from a one-sixth dynamically scaled three-bladed articulated rotor model of the CH-47D helicopter which was tested by Boeing Helicopter Company in their wind tunnel [5]. In the experiment, the vibratory hub loads were measured in the rotating frame using a strain-gauge balance located under the rotor hub. Therefore, for this three-bladed rotor, the vibratory hub loads of interest are the 3P vertical and the 2P and 4P rotating inplane hub shears. The vibratory hub moment components for this rotor are small, and these are not considered in the correlation study. In order to apply the nonlinear unsteady aerodynamic model [14,15], static characteristics for the VR-12 airfoil were used. Basic trim controls are calculated corresponding to the wind tunnel conditions with a specified rotor thrust, advance ratio, and shaft tilt angle. For wind tunnel trim calculation, the cyclic flapping angles are trimmed to zero.

Figure 1 shows the correlation of the 3P vertical hub shear over a range of forward speeds with a thrust coefficient-solidity ratio of 0.08 (where C_T is the rotor thrust coefficient, and σ is the rotor solidity ratio). Calculated results are shown for three aerodynamic models: (1) quasi-steady aerodynamics and linear inflow model of Drees [19], (2) nonlinear unsteady aerodynamics (including dynamic stall) and Drees inflow model, and (3) nonlinear unsteady aerodynamics and free wake model. Predicted results obtained using nonlinear aerodynamics and free wake modeling agree quite well with measured data at low speed as well as high speed flight regimes. At higher speeds, the sharp rise in the 3P vertical hub shear is attributed to dynamic stall, and this effect is reflected in the analytical results using nonlinear aerodynamics. The sharp peak in the 3P vertical hub shear in the transition flight regime (around 40 knots) is satisfactorily predicted using free wake analysis. Figure 2 shows the correlation of the 2P rotating inplane hub shear using all three aerodynamic models. Again, the correlation with test data is quite good for the complete range of forward speeds shown. The small peak in the 2P inplane hub shear in the transition flight regime is predicted using the free wake analysis. Correlation of the 4P rotating inplane hub shear is shown in Figure 3. This figure shows that results obtained by three analytical models are quite identical for forward speeds below 135 knots. At higher forward speeds, the results obtained with nonlinear aerodynamics and free wake model yield better correlation with experimental data. Subsequent results are all calculated using nonlinear aerodynamics and free wake model.

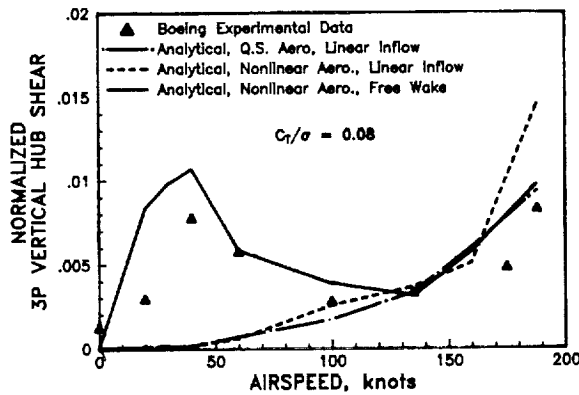


Fig. 1 Correlation of 3P vertical hub shears.

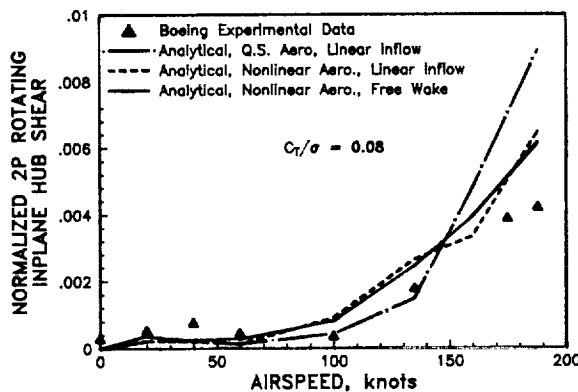


Fig. 2 Correlation of 2P rotating inplane hub shear.

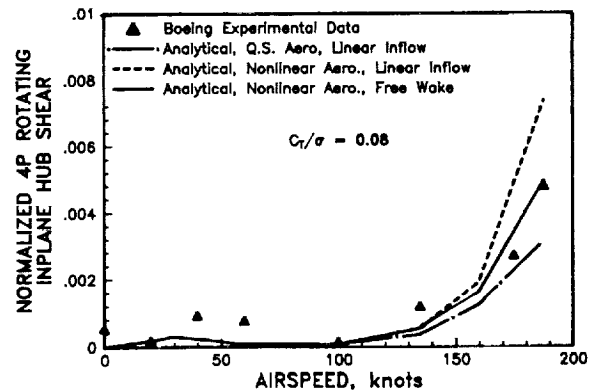


Fig. 3 Correlation of 4P rotating inplane hub shear.

For the flight conditions considered above, optimal closed-loop HHC is introduced in the analysis to suppress the three vibratory hub shears. Since three HHC components are available to control the three vibratory hub shears, the HHC controller is extremely effective: all three vibratory hub shear components are suppressed by more than 99 percent. The 3P swashplate motions required by the HHC controller to suppress these vibratory hub shears are presented in Figure 4. Note that the HHC inputs are transformed to the higher harmonic swashplate motions in the collective, longitudinal cyclic, and lateral cyclic modes. Figure 4 shows that, except in the transition flight regime, the amplitudes required by the longitudinal and lateral cyclic modes are higher than the collective amplitudes. The actuator power required by the HHC system, expressed in terms of the actuator power index, is presented in Figure 5. The actuator power index is large in the transition flight condition (around 25 knots) and again grows at high forward speeds. Noticeably, the actuator power index reflects the level of vibratory shear being suppressed at the rotor hub.

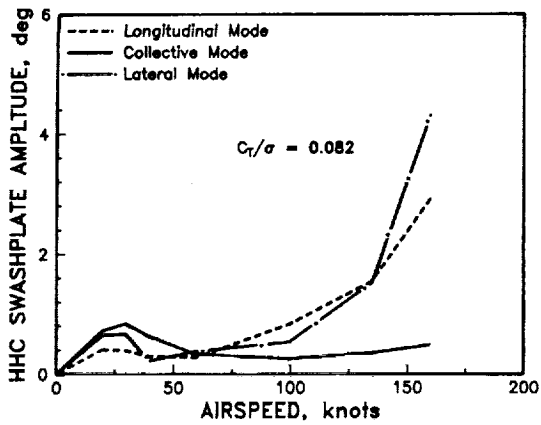


Fig. 4 Variation of HHC swashplate motion with forward speed.

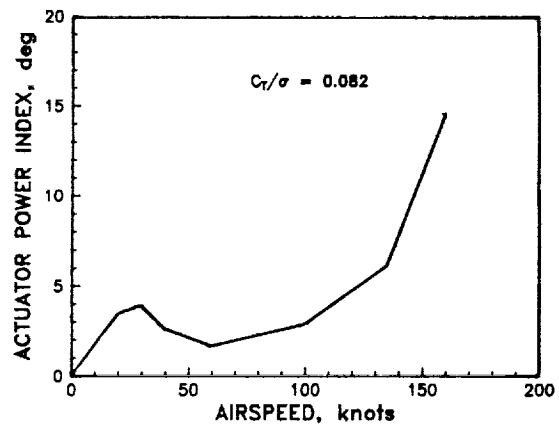


Fig. 5 Variation of HHC actuator power with forward speed.

3.2. Articulated vs. Hingeless Rotors

The above correlations are made for a typical articulated rotor system. Next, the vibration suppressions of two hingeless rotor configurations are analyzed and compared with results of the articulated rotor system. These hingeless rotors represent respectively a soft-inplane (lag frequency = 0.71P) and a stiff-inplane (lag frequency = 1.4P) configuration (both have a fundamental flap frequency of 1.1P). For these results, wind tunnel flight conditions are simulated with forward speed ranging from 0 to 188 knots at a C_T/σ of 0.08. Figure 6 shows the 3P vertical hub shears variation with forward speeds for three rotor systems. Below 100 knots, the calculated 3P vertical hub shears for these rotors are quite comparable. At higher speeds, the 3P vertical hub shear for the stiff-inplane rotor increases rapidly with speed, while this component remains the lowest for the articulated rotor system. Variation of the 2P rotating inplane hub shear with forward speeds for these three rotors is shown in Figure 7. For forward speeds below 135 knots, the articulated and soft-inplane hingeless rotors exhibit similar variations; whereas at higher speeds, this vibratory hub shear component for the soft-inplane rotor is about 30 percent lower than that for the articulated rotor. For the stiff-inplane rotor, this vibratory hub shear component increases considerably for forward speeds above 100 knots. This is understandable in that the blade fundamental lag mode frequency for the stiff-inplane rotor of 1.4P is closer to the resonant frequency of 2P than the other two rotor systems. Figure 8 shows the 4P rotating inplane hub shears. The magnitudes of this high frequency hub shear are much smaller than those of the low frequency 2P hub shear and are quite similar for all three rotor systems.

Next, HHC inputs are applied to suppress the vibratory hub shear components for these rotor configurations. *Because the HHC system is quite effective in suppressing completely the 3P vertical and the 2P and 4P rotating inplane hub shears, the controlled vibratory hub shears are not shown.* Even though the vibratory hub moments for the hingeless rotor are not small, these are not controlled so that subsequent HHC results can be compared directly with those obtained earlier for the articulated rotor.

Figure 9 shows the actuator power index required by the HHC system at different forward speeds. For the stiff-inplane hingeless configuration operating above 100 knots, HHC inputs required to suppress the vibratory hub shears become very large, and the problem associated with the convergence of the numerical solution hinders any more results. For moderate to high forward speeds shown, the power index for the soft-inplane hingeless rotor is larger than that required for the articulated rotor. It is interesting to note that in the transition flight regime, the actuator power index is the largest for the soft-inplane rotor even though the vibratory hub loads are the largest for the stiff-inplane configuration. However, for forward speeds above 140 knots, the power index for the soft-inplane hingeless rotor becomes lower than that for the articulated rotor system. In fact, at 160 knots, the power index for the soft-inplane hingeless rotor is less than half that of the articulated rotor. For forward speeds above 50 knots, the actuator power index required by the stiff-inplane hingeless rotor is the largest among the three rotor systems considered.

3.3. Sensitivity Analysis

Next, the sensitivity of the uncontrolled vibratory hub loads and actuator power for hingeless rotors, with respect to blade design parameters and blade thrust, is examined. For this simulation, a four-bladed soft-inplane hingeless rotor is used. The structural characteristics of this rotor blade are similar to those of the three-bladed soft-inplane hingeless rotor considered earlier; i.e., the blade fundamental flap and lag mode frequencies are 1.1P and 0.7P, respectively. Propulsive trim with steady level flight is simulated for forward speed of 40 knots, corresponding to a rotor advance ratio of 0.09 and a C_T/σ of 0.08. This airspeed corresponds to the transition flight regime where the rotor would experience a high level of vibration. The closed-loop HHC controller is now configured to suppress the 4P vertical, the 3P and 5P rotating inplane hub shears, and the 3P and 5P rotating hub moments.

3.3.1. Blade Torsion Stiffness

Blade torsion frequency is varied by adjusting blade torsion stiffness of the inboard section. In this simulation, the blade rotating fundamental torsion frequency is varied from 3P to 7P, and the baseline value is 4.5P. Figure 10(a) shows the uncontrolled vibratory hub shears with blade torsion frequency. For most of the range of frequencies shown, the rotor vibratory hub shear components are quite insensitive to the blade torsion stiffness. For frequencies below 4P, however, there is a considerable reduction in the 4P vertical hub shear and a moderate increase in the 3P inplane hub shear. The increase in the 3P inplane shear component is probably due to resonance. The vibratory hub moments are presented in Figure 10(b), where the 3P hub moment is shown to increase moderately with blade torsion stiffness. The 5P hub moment is small, however, compared to the 3P component and is quite insensitive to blade torsion stiffness. The actuator power variation with blade torsion frequency is shown in Figure 10(c). Note that the power index is lowest at the blade torsion frequency of about 3.85P, at which the actuator power index is less than half that at the torsion frequency of 7P.

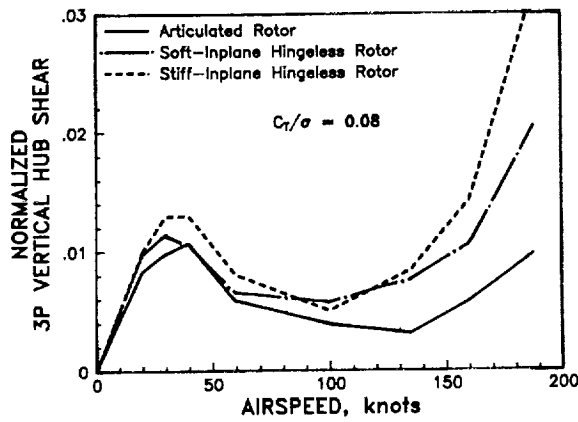


Fig. 6 Variation of 3P vertical hub shear with forward speed for different rotors.

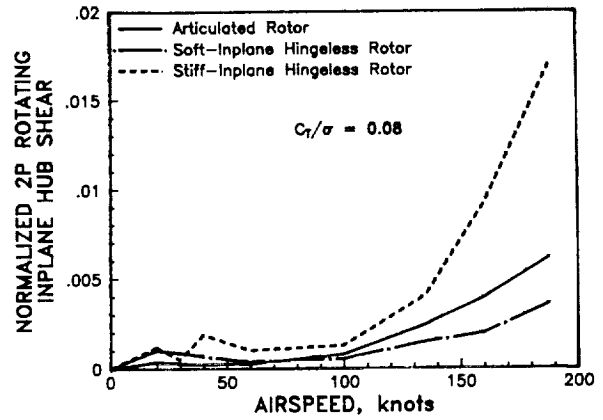


Fig. 7 Variation of 2P rotating inplane hub shear with forward speed for different rotors.

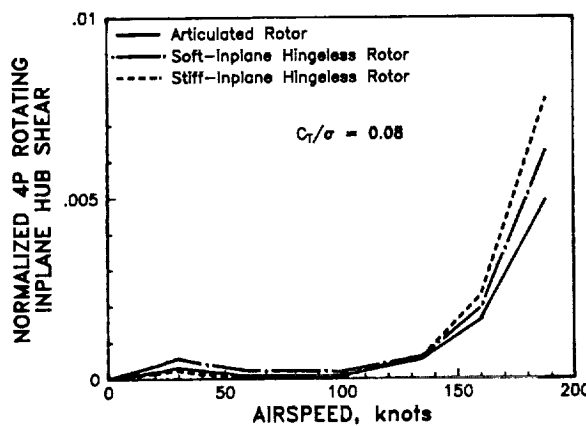


Fig. 8 Variation of 4P rotating inplane hub shear with forward speed for different rotors.

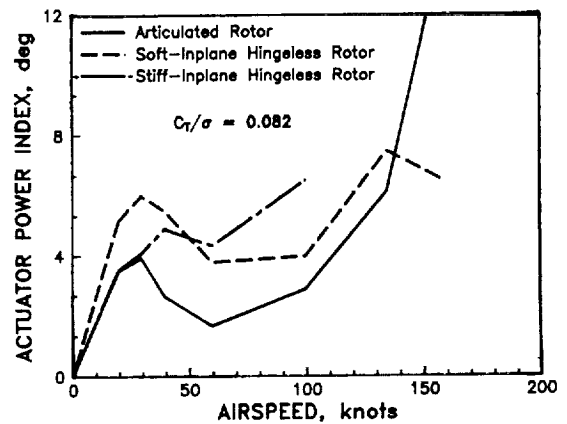


Fig. 9 Variation of actuator power with forward speed for different rotors.

3.3.2. Blade Bending Stiffnesses

Blade bending stiffnesses in the flapwise and chordwise directions are varied to study their effects on the vibratory hub loads and the actuator power. Blade bending stiffness in the flapwise direction affects the blade elastic flap modes, and its variations are presented in terms of the blade second rotating flap mode frequency. Figure 11(a) shows the uncontrolled vibratory hub shears variation with blade flap mode frequency, and the baseline value is 2.88P. Variation of the flapwise stiffness affects all three vibratory hub shear components. The 4P vertical hub shear is at a minimum when the blade frequency is about 3P, while the 3P inplane hub shear is minimum when the blade frequency is 2.65P. The 5P inplane hub shear component is small when compared to the other two components, and its magnitude decreases steadily with an increase in flap stiffness. Variations of the 3P and 5P hub moment with blade flap bending stiffness are shown in Figure 11(b). Within the range of flap frequencies shown, the 5P hub moment increases sharply as the flap frequency is reduced below 2.6P, while the 3P hub moment reaches a minimum at this frequency value. In Figure 11(c), the actuator power remains constant for the range of flap frequencies above 2.9P and increases sharply for the range of flap frequencies below this value.

Variation of the blade chordwise stiffness is presented in terms of the blade second rotating lag mode frequency, and the baseline value is 5.8P. The uncontrolled vibratory hub shears are presented in Figure 12(a). For this rotor configuration, the vibratory hub shears are quite sensitive to placements of the blade second lag mode frequencies. The magnitude amplifications of the hub shear are quite pronounced as the blade frequency is placed at the corresponding harmonic. It is interesting to note that the resonant conditions exist not only for the inplane shears but also for the vertical component. In fact, at resonance the 4P vertical hub shear increases by four and one half times from the baseline value. Magnitude amplification is also visible from Figure 12(b) where the vibratory hub moments are presented. This figure shows that the 5P hub moment increases noticeably as the lag frequency approaches 5P, while the effect of lag stiffness on the 3P hub moment is small. The actuator power index variation shown in Figure 12(c) indicates that minimum power required is achieved by placing blade lag frequencies either at 3.6P or at 6.2P away from the resonant frequencies.

3.3.3. Blade Linear Pretwist

The blade pretwist value is typically selected based on the rotor aerodynamic performance in both hover and forward flight. For this study, however, the blade linear pretwist is varied so that its effects on the vibratory hub loads and actuator power can be assessed. Blade pretwist redistributes blade steady airloads in the spanwise direction and introduces flap-lag coupling. The variation in blade pretwist considered in this study ranges from 0 to -16 degrees, with the baseline configuration having a -8 degrees of pretwist. Figures 13(a) and 13(b) show, respectively, the vibratory hub shears and moments with blade pretwist. These show that the 4P vertical and the 3P inplane hub shears and the two hub moment components all decrease with increase in blade pretwist. The 5P inplane hub shear is small and increases slightly with an increase in blade pretwist. The actuator power is shown in Figure 13(c), where a reduction of 20 percent in the actuator power is achieved with a blade pretwist of -16 degrees as compared to an untwisted blade.

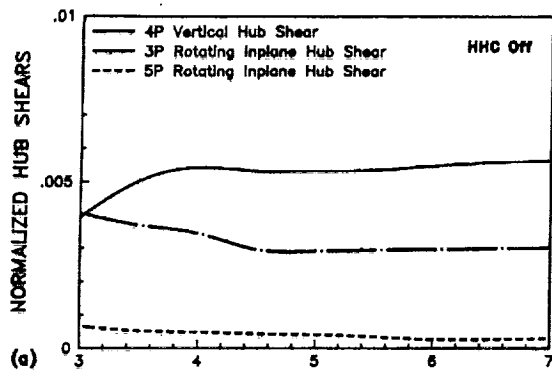


Fig. 10(a) Effects of blade torsion stiffness on the vibratory hub shear ($V = 40$ knots, $C_T/\sigma = 0.08$).

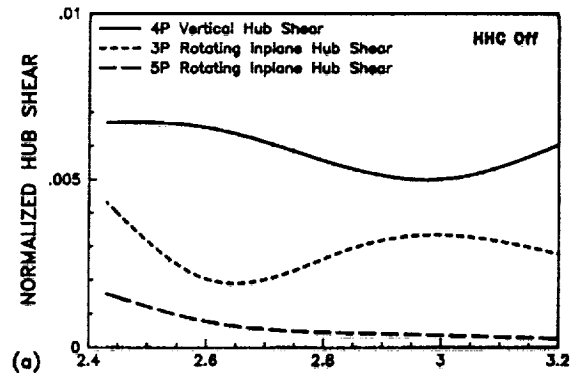


Fig. 11(a) Effects of blade flap stiffness on the vibratory hub shear ($V = 40$ knots, $C_T/\sigma = 0.08$).

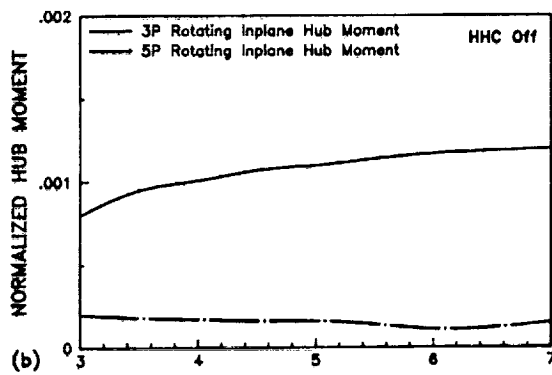


Fig. 10(b) Effects of blade torsion stiffness on the vibratory hub moment ($V = 40$ knots, $C_T/\sigma = 0.08$).

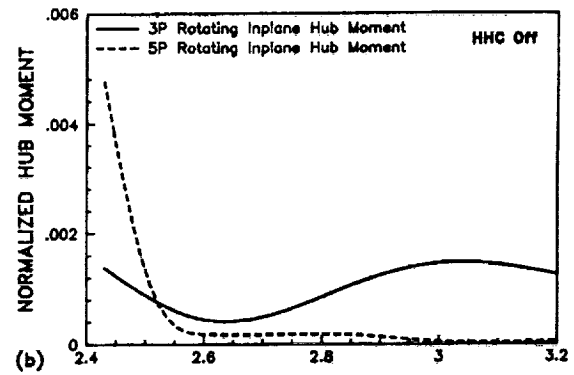


Fig. 11(b) Effects of blade flap stiffness on the vibratory hub moment ($V = 40$ knots, $C_T/\sigma = 0.08$).

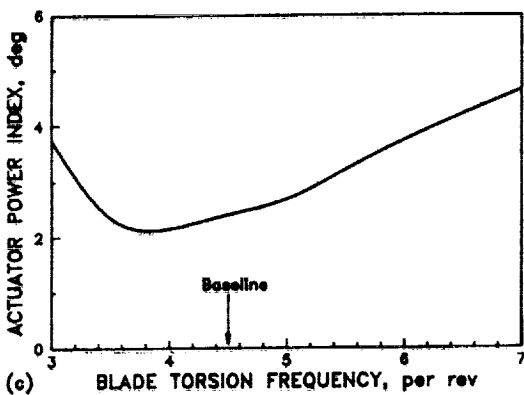


Fig. 10(c) Effects of blade torsion stiffness on the HHC actuator power ($V = 40$ knots, $C_T/\sigma = 0.08$).

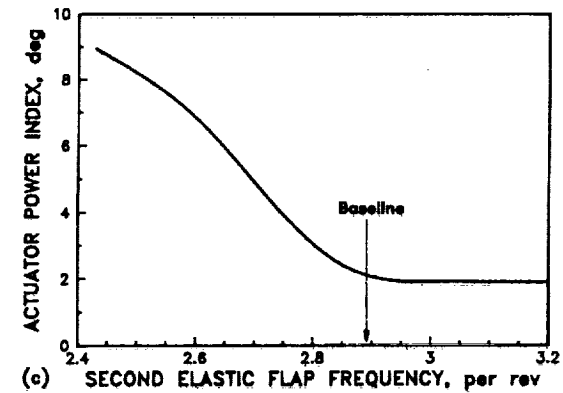


Fig. 11(c) Effects of blade flap stiffness on the HHC actuator power ($V = 40$ knots, $C_T/\sigma = 0.08$).

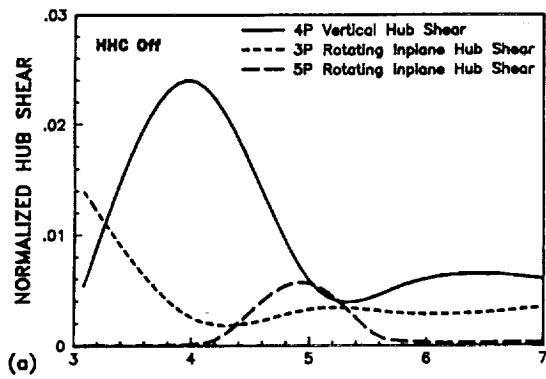


Fig. 12(a) Effects of blade lag stiffness on the vibratory hub shear ($V = 40$ knots, $C_T/\sigma = 0.08$).

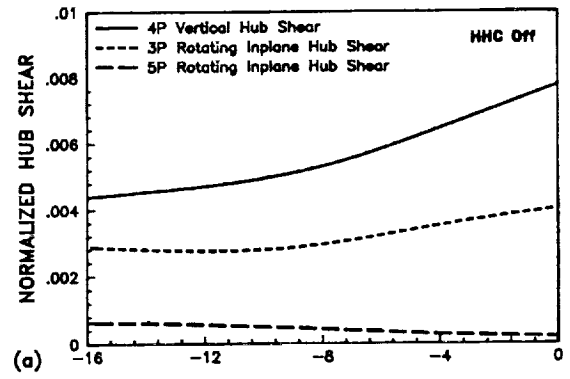


Fig. 13(a) Effects of blade linear pretwist on the vibratory hub shear ($V = 40$ knots, $C_T/\sigma = 0.08$).

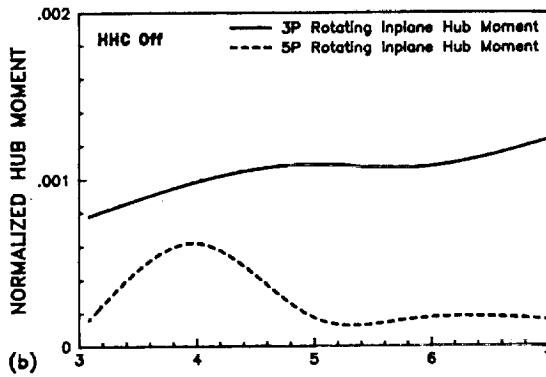


Fig. 12(b) Effects of blade lag stiffness on the vibratory hub moment ($V = 40$ knots, $C_T/\sigma = 0.08$).

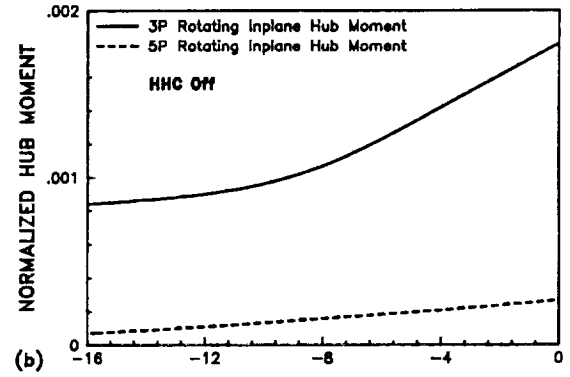


Fig. 13(b) Effects of blade linear pretwist on the vibratory hub moment ($V = 40$ knots, $C_T/\sigma = 0.08$).

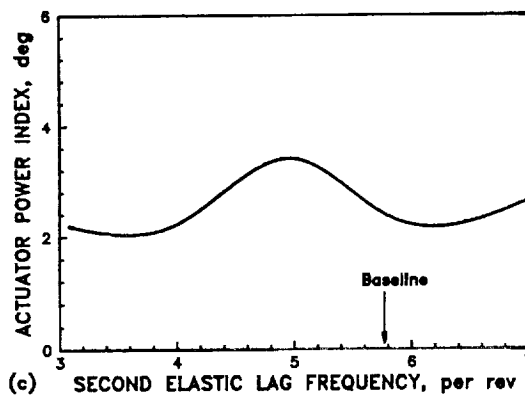


Fig. 12(c) Effects of blade lag stiffness on the HHC actuator power ($V = 40$ knots, $C_T/\sigma = 0.08$).

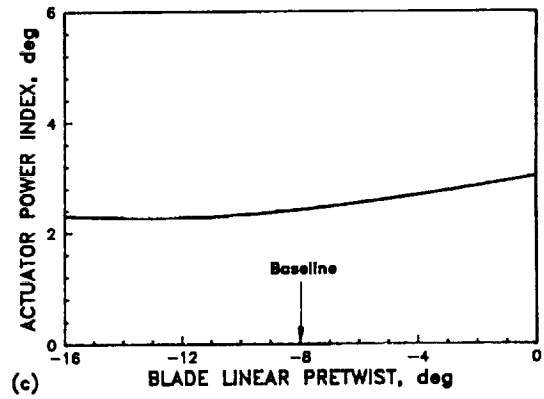


Fig. 13(c) Effects of blade linear pretwist on the HHC actuator power ($V = 40$ knots, $C_T/\sigma = 0.08$).

3.3.4. Blade Chordwise Center-of-Gravity Offset

Blade chordwise center-of-gravity (c.g.) offset from the elastic axis introduces inertial coupling between the flap and torsion modes. For this study, the elastic axis is assumed to be at the quarter-chord axis, and a positive c.g. offset represents the blade center of mass placed ahead of the quarter-chord toward the blade leading edge. The baseline rotor configuration has no offset. Figures 14(a) and 14(b) show that the 4P vertical and the 3P inplane hub shears and the 3P hub moment are all reduced as the blade c.g. is shifted forward of the elastic axis. The 5P hub shear and 5P hub moment are small compared to the other vibratory hub load components and both increase slightly as the blade chordwise c.g. is moved ahead of the elastic axis. From Figure 14(c), the actuator power increases sharply as the blade c.g. is placed by more than 2 percent of chord length ahead of the elastic axis and increases slightly as the blade c.g. is placed behind the elastic axis. In fact, the actuator power is lowest when the blade c.g. is placed 2 percent of chord ahead of the elastic axis.

3.3.5. Offset of Elastic Axis from Quarter-Chord Axis

The offset of elastic axis from the blade quarter-chord introduces aerodynamic pitch-flap coupling, and its effects on the vibratory hub loads and HHC system are examined. The offset is positive when the blade elastic axis is placed ahead of the quarter-chord. For the baseline rotor, the elastic axis is at quarter-chord (zero offset). Figures 15(a) and 15(b) show the variations of the vibratory hub loads with offset of elastic axis from quarter-chord. The variations of vibratory hub loads are quite similar to those observed when the blade c.g. is varied with respect to the elastic axis location. Figure 15(c) shows the actuator power variation with the elastic axis location, and again a similar behavior is observed as that shown in Figure 14(c). Placing the elastic axis in front of quarter-chord helps reduce the dominant components of vibratory hub load. A minimum actuator power is achieved by placing the elastic axis 3 percent of chord length ahead of quarter-chord. At this minimum point, a 17 percent reduction in actuator power is achieved from the baseline value.

It is interesting to note from the sensitivity study that the blade design parameters chosen for the baseline blade configuration, with the exception of the blade pretwist, happen to be quite close to the optimum values. Also, directing these parameters toward an optimum value would result in only a small reduction, of less than 20 percent, in the actuator power.

3.3.6. Blade Thrust

Blade thrust, expressed in term of rotor thrust coefficient-solidity ratio, C_T/σ , is varied from 0.06 to 0.12, and the results are shown in Figures 16(a)-(c). Figure 16(a) and 16(b) show that all the vibratory hub load components increase noticeably with an increase in blade thrust. The actuator power variation is presented in Figure 16(c) showing that at high thrust, $C_T/\sigma = 0.12$, the power required is twice that for the baseline case ($C_T/\sigma = 0.08$). Within the range of blade thrust shown, the actuator power varies almost linearly with the thrust value.

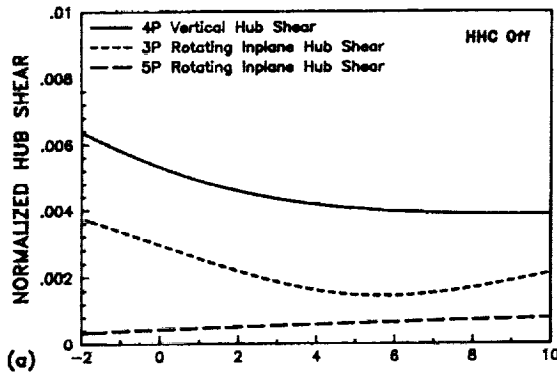


Fig. 14(a) Effects of blade center-of-mass offset from elastic axis on the vibratory hub shear ($V = 40$ knots, $C_T/\sigma = 0.08$).

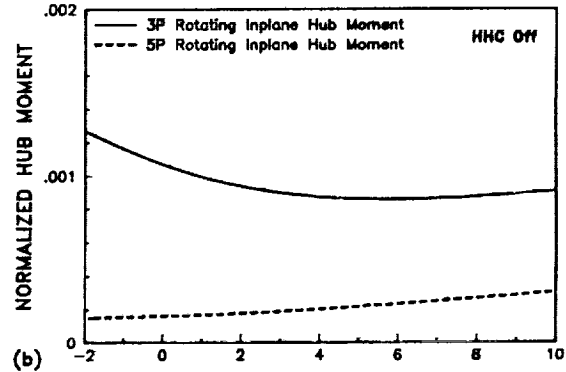


Fig. 14(b) Effects of blade center-of-mass offset from elastic axis on the vibratory hub moment ($V = 40$ knots, $C_T/\sigma = 0.08$).

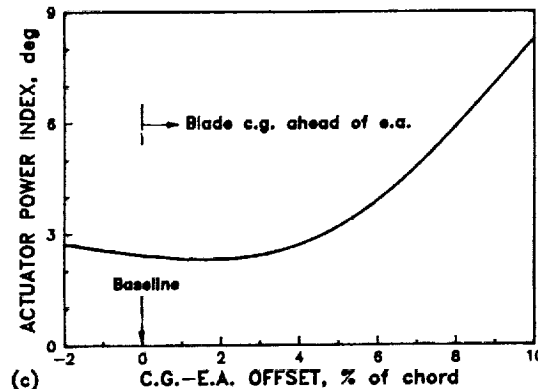


Fig. 14(c) Effects of blade center-of-mass offset from elastic axis on the HHC actuator power ($V = 40$ knots, $C_T/\sigma = 0.08$).

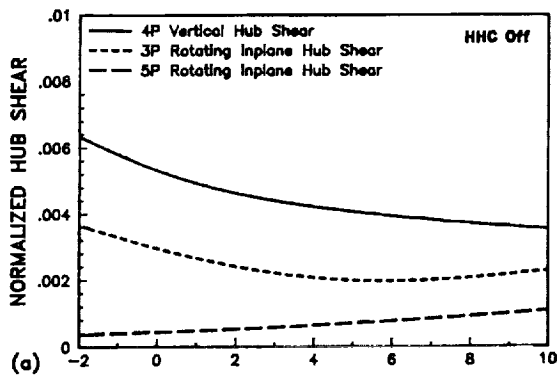


Fig. 15(a) Effects of blade elastic axis offset from quarter-chord on the vibratory hub shear ($V = 40$ knots, $C_T/\sigma = 0.08$).

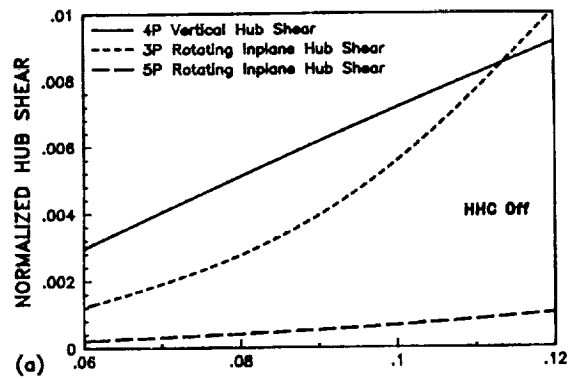


Fig. 16(a) Effects of rotor thrust on the vibratory hub moment ($V = 40$ knots, $C_T/\sigma = 0.08$).

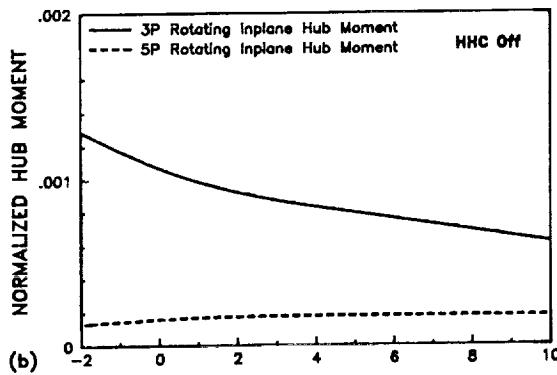


Fig. 15(b) Effects of blade elastic axis offset from quarter-chord on the vibratory hub moment ($V = 40$ knots, $C_T/\sigma = 0.08$).

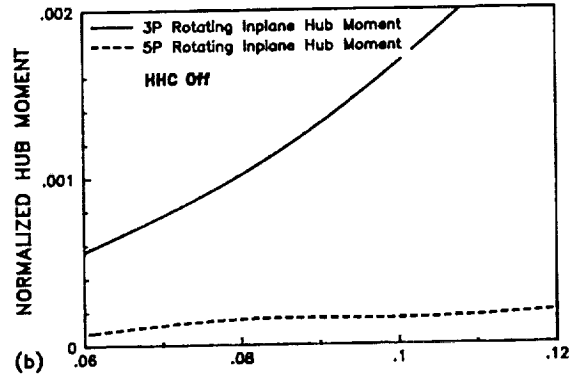


Fig. 16(b) Effects of rotor thrust on the vibratory hub shear ($V = 40$ knots, $C_T/\sigma = 0.08$).

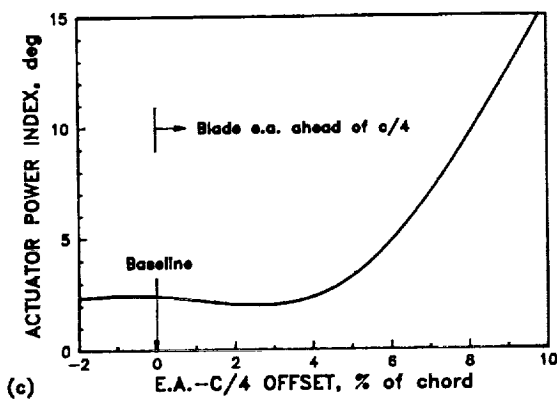


Fig. 15(c) Effects of blade elastic axis offset from quarter-chord on the HHC actuator power ($V = 40$ knots, $C_T/\sigma = 0.08$).

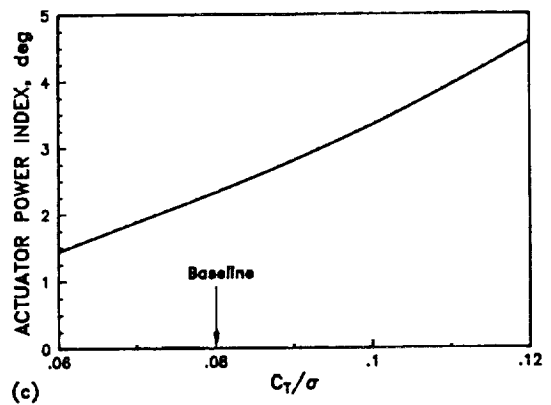


Fig. 16(c) Effects of rotor thrust on the HHC actuator power ($V = 40$ knots, $C_T/\sigma = 0.08$).

4. CONCLUSIONS

An analytical formulation has been developed to calculate the vibratory hub loads of helicopter rotors in forward flight and the corresponding higher harmonic control inputs to minimize these loads. The predicted uncontrolled vibratory hub loads are correlated with experimental data obtained from a scale model rotor. Based on the correlation studies for an articulated rotor and the simulations of two generic hingeless rotors, the following conclusions are drawn:

1. Good correlation of analytically predicted vibratory hub loads with experimental data was obtained. Refined unsteady aerodynamics including nonlinear effects and dynamic stall help improve the correlation at high forward speeds, while the inclusion of the free wake model improves the correlation in the transition flight regime.

2. Closed-loop HHC is effective in suppressing nearly all the rotor vibratory hub shears for the articulated and soft-inplane hingeless rotors from hover to 160 knots.

3. The HHC actuator amplitudes and power required are proportional to the predicted vibratory hub loads and increase substantially at high forward speeds. For forward speeds below 140 knots, the actuator power for the articulated rotor is less than that for the soft-inplane hingeless rotor; whereas at 160 knots, the actuator power for the soft-inplane hingeless rotor is about half that of the articulated rotor. The actuator power for the stiff-inplane hingeless rotor is generally greater than that for the other rotors.

From the parametric HHC study of a four-bladed soft-inplane hingeless rotor operating in the transition flight regime, the following conclusions are drawn:

4. The actuator power is quite sensitive to the blade torsion stiffness, while the baseline vibratory hub loads are less sensitive. Placing the blade torsion frequency at 3.85P results in a minimum actuator power.

5. Placing the blade second elastic flap frequency above 2.9P helps reduce the actuator power.

6. The uncontrolled vibratory hub loads are sensitive to the placement of the blade second elastic lag frequency. Placing the blade second elastic lag frequency at 3.5P or at 6.2P helps reduce the actuator power.

7. An increase in blade linear pretwist reduces the actuator power.

8. Placing the blade center of mass 2 percent of chord length ahead of the elastic axis and the elastic axis 3 percent of chord length forward of the quarter-chord axis reduces the actuator power.

9. The uncontrolled vibratory hub loads and the actuator power increase with the thrust value.

REFERENCES

1. I. Chopra and J. C. McCloud III, A numerical simulation study of open-loop, closed-loop and adaptive multicyclic control systems. *J. Am. Helicopter Soc.* **28**, 1, pp. 63-77 (1983).
2. J. Shaw, Higher harmonic blade pitch control: a system for helicopter vibration control. Ph.D., Dissertation, Massachusetts Institute of Technology, MA (1980).
3. K. Nguyen and I. Chopra, Actuator power requirement for higher harmonic control (HHC) systems. *2nd Int. Conf. Rotorcraft Basic Research*, College Park, Maryland (1988).
4. C. E. Hammond, Wind tunnel results showing rotor vibratory loads reduction using higher harmonic blade pitch. *J. Am. Helicopter Soc.* **28**, 1, pp. 10-15 (1983).
5. J. Shaw, N. Albion, E. J. Hanker and R. S. Teal, Higher harmonic control: wind tunnel demonstration of fully effective vibratory hub forces suppression. *J. Am. Helicopter Soc.* **34**, 1, pp. 14-25 (1989).
6. G. Lehmann, The effect of higher harmonic control (HHC) on a four-bladed hingeless model rotor. *Vertica* **9**, 273-284 (1985).
7. E. R. Wood, R. W. Powers, C. H. Cline and C. E. Hammond, On developing and flight testing a higher harmonic control system. *J. Am. Helicopter Soc.* **30**, 1, pp. 3-20 (1985).
8. W. Miao, S. B. R. Kottapalli and H. M. Frye, Flight demonstration of higher harmonic control (HHC) on S-76. *Proc. 42nd A. Forum American Helicopter Society*, Washington D.C., pp. 777-789 (1986).
9. M. Polychroniadis and M. Achache, Higher harmonic control: flight tests of an experimental system on SA349 research Gazelle. *Proc. 42nd A. Forum American Helicopter Society*, Washington D.C., pp. 811-820 (1986).
10. W. Johnson, Recent development in the dynamics of advanced rotor systems. NASA TM-86669 (1985).
11. B. Panda and I. Chopra, Dynamics of composites rotor blades in forward flight. *Vertica* **11**, 187-210 (1987).
12. A. L. Dull, Aeroelastic stability of bearingless rotor in forward flight. *J. Am. Helicopter Soc.* **33**, 4, pp. 38-46 (1988).
13. J. W. Lim and I. Chopra, Aeroelastic optimization of a helicopter rotor. *J. Am. Helicopter Soc.* **34**, 1, pp. 52-62 (1989).
14. J. G. Leishman and T. S. Beddoes, A generalised model for unsteady aerodynamic behaviour and dynamic stall using the indicial method. *Proc. 42nd A. Forum American Helicopter Society*, Washington D.C., pp. 243-265 (1986).
15. J. G. Leishman, Validation of approximate indicial aerodynamic functions for two-dimensional subsonic flow. *J. Aircraft* **25**, pp. 914-922 (1988).
16. W. Johnson, A comprehensive analytical model of rotor aerodynamics and dynamics, part I: analysis and development. NASA TM-81182 (1980).
17. J. C. Biggers and J. L. McCloud III, A note on multicyclic control by swashplate oscillation. NASA Technical Memorandum 78475, April (1978).
18. R. H. Warring, *Hydraulic Handbook*. Gulf Publishing Company, Houston, Texas (1983).
19. W. Johnson, *Helicopter Theory*. Princeton University Press, Princeton, New Jersey (1980).



Report Documentation Page

1. Report No. NASA TM-103846	2. Government Accession No.	3. Recipient's Catalog No.	
4. Title and Subtitle Application of Higher Harmonic Control to Hingeless Rotor Systems		5. Report Date March 1991	6. Performing Organization Code
		8. Performing Organization Report No. A-90263	10. Work Unit No. 505-59-36
7. Author(s) Khanh Nguyen and Inderjit Chopra*		11. Contract or Grant No.	
		13. Type of Report and Period Covered Technical Memorandum	
9. Performing Organization Name and Address Ames Research Center Moffett Field, CA 94035-1000		14. Sponsoring Agency Code	
12. Sponsoring Agency Name and Address National Aeronautics and Space Administration Washington, DC 20546-0001			
15. Supplementary Notes Point of Contact: Khanh Nguyen, Ames Research Center, MS T-42, Moffett Field, CA 94035-1000 (415) 604-6668 or FTS 464-6668 Submitted to <i>Vertica</i> , October 1990. *University of Maryland, College Park, Maryland 20742			
16. Abstract <p>A comprehensive analytical formulation has been developed to predict the vibratory hub loads of a helicopter rotor system in forward flight. The analysis is used to calculate the optimal higher harmonic control inputs and associated actuator power required to minimize these hub loads. The present formulation is based on a finite element method in space and time. A nonlinear time domain, unsteady aerodynamic model is used to obtain the airloads, and the rotor induced inflow is calculated using a nonuniform inflow model. Predicted vibratory hub loads are correlated with experimental data obtained from a scaled model rotor. Results of a parametric study on a hingeless rotor show that blade flap, lag and torsion vibration characteristics, offset of blade center of mass from elastic axis, offset of elastic axis from quarter-chord axis, and blade thrust greatly affect the higher harmonic control actuator power requirement.</p>			
17. Key Words (Suggested by Author(s)) Higher harmonic control Hingeless rotors Actuator power requirement Comprehensive analytical formulation		18. Distribution Statement Unclassified-Unlimited Subject Category - 01	
19. Security Classif. (of this report) Unclassified	20. Security Classif. (of this page) Unclassified	21. No. of Pages 16	22. Price A02

